International Journal of Nanomedicine

Dovepress
Taylor & Francis Group

Open Access Full Text Article

ORIGINAL RESEARCH

Formulation and Evaluation of VCAM-1-Targeted Methotrexate Lipid Nanoparticles for Rheumatoid Arthritis Therapy

Ren Na[1,*], Jianmei Jing[2,*], Hua Yang[3,*], Ye Li[3], Xiaofeng Yuan[1], Xue Sun[4], Jiangfan Han[1], Jiajun Wang[1], Zhenhua Tong[4], Guangbin He[2], Weiliang Ye[1]

[1]Department of Pharmaceutics, School of Pharmacy, Fourth Military Medical University, Xi'an, 710032, People's Republic of China; [2]Department of Ultrasound Diagnosis, Xijing Hospital, Fourth Military Medical University, Xi'an, 710038, People's Republic of China; [3]Department of Medical Affairs, No. 968 Hospital of Chinese People's Liberation Army, Jinzhou, 121000, People's Republic of China; [4]Department of Pharmacy, General Hospital of Northern Theater Command, Shenyang, 110016, People's Republic of China

*These authors contributed equally to this work

Correspondence: Guangbin He; Weiliang Ye, Email guangbinhe@fmmu.edu.cn; yaojixue@fmmu.edu.cn

Objective: Methotrexate (MTX) is widely used for rheumatoid arthritis (RA) but has poor targeting and significant side effects. This study developed MTX-loaded lipid nanoparticles modified with PVCAM-1 peptide (MTX@LNP-PVCAM-1) to enhance targeting and reduce toxicity.

Methods: MTX@LNP-PVCAM-1 was prepared using the thin-film dispersion method. Particle size and morphology were assessed by dynamic light scattering (DLS) and transmission electron microscopy (TEM). Biocompatibility was tested using human umbilical vein endothelial cells (HUVEC) and hemolysis assays. Cellular uptake was examined via fluorescence microscopy, while cytotoxicity and cell migration inhibition were evaluated using CCK-8 and scratch assays. Inflammatory cytokines (IL-1β, IL-6) were measured by ELISA. Distribution in adjuvant-induced arthritis (AIA) rats was observed using in vivo imaging, and safety and anti-inflammatory effects were assessed through blood tests, paw volume, joint scores, and histology.

Results: MTX@LNP-PVCAM-1 had an average particle size of 168.5 nm, PDI of 0.142, and zeta potential of −12.1 mV, with spherical morphology. It exhibited pH responsiveness and good biocompatibility. Compared with unmodified MTX@LNP, PVCAM-1 surface modification significantly increased cellular uptake efficiency ($p<0.05$) and more effectively inhibited the growth ($p<0.05$), migration ($p<0.05$), and secretion of inflammatory cytokines (significantly reduced levels of IL-1β and IL-6, $p<0.05$) of synovial fibroblasts. In animal experiments, the accumulation of MTX@LNP-PVCAM-1 in inflamed sites was significantly higher than that of MTX@LNP ($p<0.05$), demonstrating good targeting. Moreover, it enhanced the anti-inflammatory effects of methotrexate in AIA rats, significantly reducing paw swelling ($p<0.05$) and joint clinical scores ($p<0.05$). Importantly, it had no significant effect on the blood routine indicators of rats ($p>0.05$), indicating no obvious toxicity.

Conclusion: MTX@LNP-PVCAM-1 combines passive and active targeting, delivering MTX efficiently to inflamed sites and reducing toxicity. This approach enhances anti-inflammatory effects in AIA rats, offering a potential strategy for low-toxicity RA treatment.

Keywords: synovial fibroblasts, PVCAM-1, lipid nanoparticles, methotrexate, rheumatoid arthritis

Introduction

Rheumatoid arthritis (RA) is a chronic systemic autoimmune disease with a global prevalence of approximately 1%. Although it is capable of affecting individuals of all ages, it is more common in middle-aged and elderly populations, and the incidence in females is two to three times higher than in males.[1] The typical pathological features of RA include imbalance of inflammatory cytokines, synovial hyperplasia, angiogenesis in the joint cavity, and progressive destruction of articular cartilage and bone tissue.[2] Clinically, RA is characterized by persistent joint swelling, pain, and stiffness.

Received: 3 April 2025
Accepted: 22 August 2025
Published: 8 September 2025

Severe cases may lead to disability due to joint destruction and life-threatening complications such as respiratory and cardiovascular diseases, as well as severe infections.[3–5]

The core pathological processes of RA involve synovial hyperplasia and joint destruction, in which rheumatoid arthritis synovial fibroblasts (HFLS-RA) are key effector cells mediating these lesions.[6] Under physiological conditions, healthy synovial fibroblasts (HFLS) participate in joint nutrition and repair by secreting lubricating molecules such as plasma proteins and hyaluronic acid. Normal synovium consists of 1–3 layers of HFLS and macrophages. However, during the course of RA, abnormal proliferation of HFLS leads to synovial thickening to 10–15 layers.[7] These abnormally proliferative HFLS-RA perpetuate a vicious cycle of "inflammation-proliferation-bone destruction" through sustained secretion of pro-inflammatory factors (eg, IL-1β, IL-6), pro-angiogenic factors (eg, VEGF), and matrix metalloproteinases (MMPs).[8] Nevertheless, significant gaps exist in current knowledge and theoretical foundations: Although existing research clearly identifies HFLS-RA as crucial effector cells, the precise regulatory mechanisms underlying their abnormal proliferation-such as crosstalk between upstream signaling pathways and the influence of metabolites within the microenvironment on their phenotype-remain incompletely elucidated.[9] Simultaneously, there is still a lack of systematic molecular-level analysis regarding the dynamic interconnections between the components of the "inflammation-proliferation-bone destruction" vicious cycle and its core regulatory nodes.[10]

Methotrexate (MTX), the cornerstone therapeutic agent for RA, demonstrates significant symptom improvement in 25–40% of patients when administered as monotherapy.[11] However, its clinical application is constrained by multiple limitations: variable oral bioavailability (13–76%), nonspecific systemic distribution due to lack of inflammation-targeting capacity, and potential severe adverse effects such as myelosuppression and hepatorenal toxicity with prolonged use.[12,13] Although biologic agents have expanded treatment options, challenges including immunogenicity risks, prohibitive costs, and suboptimal response in certain patient populations remain unresolved. The core research problem lies in: current therapies fail to achieve precision targeting of HFLS-RA (Rheumatoid Arthritis Synovial Fibroblasts). Agents like MTX suffer from insufficient efficacy and significant toxicity due to systemic distribution. Conversely, biologics, by targeting single inflammatory factors, struggle to disrupt the complex pathological cascade. Furthermore, critical barriers remain unaddressed for targeted delivery systems, including penetration capability within RA's complex synovial microenvironment, retention efficiency at inflammatory sites, and assurance of long-term safety.[14–16] Recent nanomedicine advances offer solutions to overcome traditional therapeutic limitations. Lipid nanoparticles (LNPs) are particularly promising due to their unique physicochemical properties: ① good biocompatibility for delivering unstable drugs or loading poorly soluble compounds; ② flexible surface modification for prolonged circulation via PEGylation or precise targeting by conjugating targeting molecules; and ③ adaptability for various administration routes, enhancing clinical application convenience.[17,18] These features make LNPs ideal carriers for optimizing RA therapy.

Notably, activated synovial fibroblasts (HFLS-RA) in the RA synovial microenvironment overexpress VCAM-1 receptors, providing a molecular basis for targeted therapy.[19,20] The CVHSPNKKC peptide, identified via phage display, shows high affinity for VCAM-1. Its conjugation with magnetic nanoparticles has demonstrated excellent targeting ability in experimental models.[21] This "smart" nanosystem, via receptor-ligand-mediated active targeting, can increase drug accumulation in diseased joints and reduce off-target effects. Currently, LNP-based combination delivery platforms (eg, co-delivering MTX and anti-inflammatory cytokines) are in preclinical research, showing potential to break traditional therapeutic limitations.[22,23]

To address the issues of low bioavailability, poor targeting, and significant toxicity associated with Methotrexate (MTX) therapy in Rheumatoid Arthritis (RA), we leveraged the carrier advantages of Lipid Nanoparticles (LNPs) and the targeting basis of the VCAM-1 receptor. We constructed PVCAM-1 peptide-functionalized MTX-loaded Lipid Nanoparticles (MTX@LNP-PVCAM-1). This system aims to achieve precision-targeted delivery to Human Fibroblast-Like Synoviocytes in RA (HFLS-RA), enhance the enrichment of MTX in the affected synovium, improve its efficacy in disrupting the "inflammation-proliferation-bone destruction" cycle, and simultaneously reduce systemic adverse effects. The experimental design is illustrated in Scheme 1. First, MTX-encapsulated lipid nanoparticles (MTX@LNP) were synthesized using lecithin, cholesterol, and methotrexate. Subsequently, the short peptide PVCAM-1 was conjugated to the surface of these nanoparticles via post-modification techniques to yield MTX@LNP-pVCAM-1. Following this, a series of in vitro and in vivo experiments were conducted to evaluate the anti-inflammatory efficacy and safety profile of

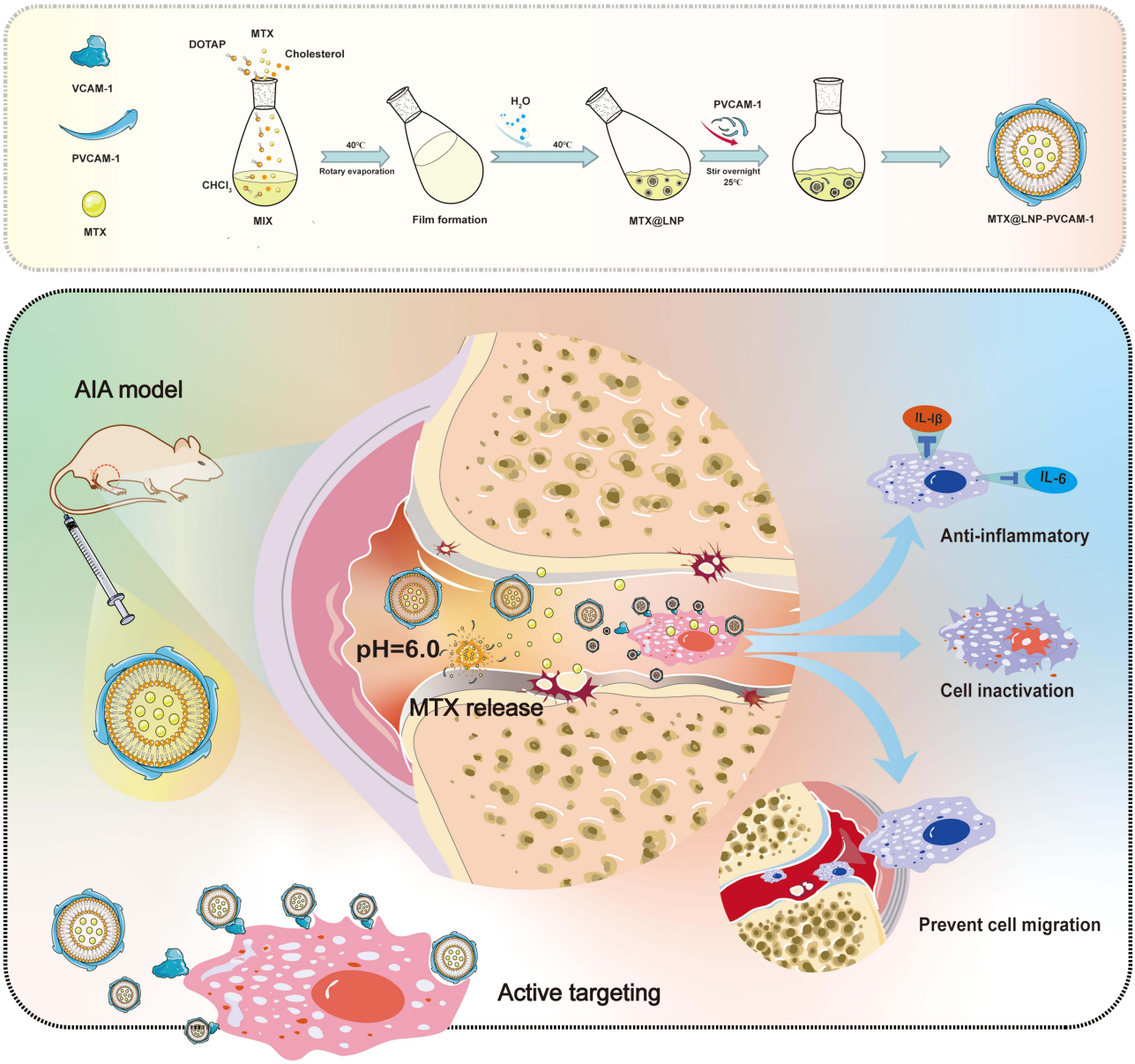

Scheme 1 Formation of MTX@LNP-PVCAM-1 and its mechanism in combination therapy for rheumatoid arthritis.

MTX@LNP-PVCAM-1. By integrating nanotechnology with the targeting peptide PVCAM-1, this study holds promise to overcome the limitations of conventional RA therapies and potentially provide RA patients with a safer and more effective therapeutic option. Precision targeting of affected joints could not only enhance drug efficacy but also reduce drug distribution to non-target tissues, thereby minimizing side effects. Furthermore, this research will also provide a theoretical basis and practical guidance for the application of nanotechnology in treating other inflammatory diseases.

Materials and Methods

Materials

1,2-distearoyl-sn-glycero-3-phosphoethanolamine-N-[methoxy(polyethyleneglycol)-5000] (DSPE-MPEG), disaturated phosphatidylcholine (DSPC), cholesterol and Lecithin (LC) were purchased from J&K Scientific Company (Beijing, China). Methotrexate (MTX) and N, N′-Disuccinimidyl carbonate (DSC) were procured from Aladdin (Shanghai, China). CVHSPNKKC (PVCAM-1) was procured from GL Biochemistry Co. 1,1-dioctadecyl-

https://doi.org/10.2147/IJN.S532163

3,3,3,3-tetramethylindotricarbonneocyiodide (DIR) was obtained from Sigma-Aldrich (China). All other chemical reagents were procured from Kehao Company (Xi'an, China). Male Sprague-Dawley rats were procured from the Laboratory Animal Centre of Air Force Military Medical University (Xi'an, China). All animal experiments were approved by the Ethics Committee of Air Force Military Medical University. This study followed the ARRIVE 2.0 guidelines for reporting in vivo animal experiments and the CONSORT Extension for Preclinical Studies to ensure rigor in experimental design and reporting.

Cell Lines and Cell Culture

The synovial fibroblasts (MH7A) and human umbilical vein endothelial cells (HUVEC) used in this study were generously provided by the Department of Rheumatology and Immunology at Xijing Hospital, Air Force Medical University. These cell lines were originally purchased from Shanghai Jingkang Bioengineering Co., Ltd. The cells were cultured in Dulbecco's Modified Eagle Medium (DMEM; Gibco, USA), supplemented with 10% fetal bovine serum (FBS; Gibco), under standard conditions of 37 °C, 5% CO_2 in a humidified incubator.

Preparation of Lipid Nanoparticles

A mixture containing 60 mg of LC, 20 mg of DSPE-MPEG, 10 mg of DSPC, and 10 mg of cholesterol was dissolved in 20 mL of chloroform.[24,25] The solution was then evaporated under reduced pressure at 30°C and 100 rpm for approximately 1 hour to form a thin film. Subsequently, 50 mg of methotrexate was dissolved in 15 mL of PBS (pH 6.0) and used to hydrate the thin film for 1 hour at 30°C and 200 rpm. The resulting solution was subjected to high-pressure homogenization to produce methotrexate-loaded lipid nanoparticles (MTX@LNP), which appeared as a pale-yellow emulsion. The MTX@LNP were stored at 4°C for further use.

To prepare PVCAM-1-modified MTX@LNP (MTX@LNP-PVCAM-1) for targeted delivery to synovial fibroblasts, a specific amount of MTX@LNP was mixed with a DSC solution and stirred at room temperature for 3 hours. Following this, a PVCAM-1 solution was added, and the mixture was stirred for an additional 3 hours. The resulting nanoparticles, designated as MTX@LNP-PVCAM-1, were functionalized with PVCAM-1 to enhance their targeting ability toward synovial fibroblasts.

Characterisation of Lipid Nanoparticles

The particle size, polydispersity index (PDI) and zeta potential of MTX@LNP and MTX@LNP-PVCAM-1 were measured by dynamic light scattering (DLS). The morphology of MTX@LNP and MTX@LNP-PVCAM-1 was observed by transmission electron microscopy (TEM). The drug loading (LD) and entrapment efficiency (EE) were measured by using high-performance liquid chromatography (HPLC). The freeze-dried LNP were mixed with methanol, and shook in water bath at 50 °C for 6 h to produce MTX. The measurement was performed in triplicate. Drug loading and entrapment efficiency was respectively calculated by the following equations:

DL (%) = (Weight of MTX in the LNP/ Weight of the LNP)×100%;

EE (%) = (Weight of MTX in the LNP/ Weight of the feeding MTX) ×100%.

Stability Studies

The stability of MTX@LNP and MTX@LNP-PVCAM-1 was evaluated under two different conditions. For in vitro storage stability, MTX@LNP and MTX@LNP-PVCAM-1 were dissolved in PBS (pH 7.4) and incubated at 4°C for 7 days. Changes in particle size and polydispersity index (PDI) were monitored over the incubation period to assess the physical stability of the nanoparticles.

For in vitro stability in simulated physiological conditions, MTX@LNP and MTX@LNP-PVCAM-1 were dissolved in PBS containing 10% fetal bovine serum (FBS) and incubated at 37°C for 24 hours. Particle size and PDI were again monitored to evaluate the ability of the nanoparticles to maintain their structural integrity in a serum-containing environment.

In vitro Drug Release Studies

The drug release profiles of lipid nanoparticles were evaluated under simulated physiological conditions to mimic extracellular and intracellular environments. In vitro release studies were conducted using PBS buffers at pH 7.4 (simulating systemic circulation) and pH 6.0 (simulating intracellular endosomal conditions). Briefly, 10 mg of MTX@LNP-PVCAM-1 or MTX@LNP was dispersed in 1 mL of release medium and transferred into a dialysis bag (molecular weight cutoff: 3.5 kDa). The dialysis bag was then submerged in 40 mL of pre-equilibrated PBS and stirred at 37°C and 120 rpm. At predetermined time intervals, 1 mL aliquots were withdrawn from the external medium and replaced with an equal volume of fresh buffer to maintain sink conditions. The cumulative release of MTX was analyzed using a Jasco high-performance liquid chromatography (HPLC) system,[26] which consists of a PU-2089 pump, an AS-2057 autosampler, an LC-Net II/ADC controller, and a Jasco MD-2015 photodiode array detector. For chromatographic analysis, a Chromolith® RP-18e reversed-phase monolithic column (100×4.6 mm internal diameter, Merck, Germany) was used, with a guard column of the same material (5×4.6 mm internal diameter) connected in front of it. The mobile phase was acetonitrile-phosphate buffer (pH 7.0, 0.1 M) at a volume ratio of 9:91, and the separation was completed within 3.5 minutes. The detection conditions were set as follows: injection volume of 50 μL, flow rate of 1.5 mL/min, and detection wavelength of 302 nm. The release kinetics were analyzed to assess the pH-responsive behavior of the nanoparticles.

Haemolytic Studies

The hemocompatibility of lipid nanoparticles (LNP and LNP-PVCAM-1) was evaluated using a hemolysis assay based on UV spectrophotometry. Briefly, 5 mL of rat blood was collected, and red blood cells (RBCs) were isolated by centrifugation at 4000 rpm for 15 minutes. The RBCs were washed three times with phosphate-buffered saline (PBS) and resuspended in PBS to prepare a 2% (v/v) RBC suspension. Different concentrations of LNP and LNP-PVCAM-1 were added to the RBC suspension, and the mixture was incubated in a 37°C incubator for 4 hours. PBS was used as the negative control, and 1% sodium dodecyl sulfate (SDS) in PBS was used as the positive control. After incubation, the samples were centrifuged at 4000 rpm for 10 minutes to separate the cells, and photos were taken to record the hemolysis status. Next, 100 μL of the supernatant from each sample was transferred to a 96-well plate, and the absorbance was measured at 540 nm using a microplate reader. The hemolysis rate was calculated using the formula:

Hemolysis rate (%) = (Sample absorbance-Negative control absorbance)/(Positive control absorbance-Negative control absorbance) × 100%.

Cytotoxicity Research

The cytotoxicity of the carrier materials LNP and LNP-PVCAM-1 was evaluated using the CCK-8 assay. HUVECs were seeded into 96-well plates at a density of 5×10^3 cells/well and incubated for 24 hours to allow cell adhesion and growth. Following incubation, the culture medium was replaced with fresh medium containing various concentrations of LNP or LNP-PVCAM-1. After an additional 24 hours of incubation, the supernatant was removed, and 100 μL of medium supplemented with 10% CCK-8 reagent was added to each well. The plates were then incubated for 2 hours at 37°C. Finally, the absorbance was measured at 450 nm using a microplate reader.

Cell-Targeting Studies

The targeting ability of MTX@LNP-PVCAM-1 and MTX@LNP toward TNF-α-activated MH7A cells and non-activated MH7A cells were visualized using fluorescence microscopy. Fluorescently labeled lipid nanoparticles, MTX@LNP-PVCAM-1-RhB and MTX@LNP-RhB, were prepared with Rhodamine B (RhB) for fluorescence tracking. The experimental procedure was as follows: MH7A cells were seeded onto coverslips placed in 24-well plates and incubated for 24 hours. Subsequently, the cells were activated with TNF-α (50 ng/mL) for 12 hours. After activation, the culture medium was replaced with fresh medium containing the fluorescent lipid nanoparticles, and the cells were further incubated for 3 hours to allow nanoparticle uptake.

As a control experiment, a 2 mg/mL solution of PVCAM-1 was pre-incubated with MH7A cells for 30 minutes prior to treatment with the lipid nanoparticles to evaluate the specificity of targeting. Following incubation, cell nuclei were stained with DAPI, then washed three times with PBS, and cellular uptake of the fluorescent lipid nanoparticles was observed using fluorescence microscopy. The cellular uptake of MTX@LNP-PVCAM-1-RhB and MTX@LNP-RhB towards the unactivated MH7A cells were also conducted similarly with the above method.

Cell Proliferation Inhibition Assay

MH7A cells were seeded into 96-well plates at a density of 8×10^3 cells/well and incubated at 37°C for 24 hours. Cells were cultured either in medium containing TNF-α (50 ng/mL) or in medium without TNF-α to establish activated and non-activated cellular conditions, respectively. After 24 hours, the culture medium was removed and replaced with fresh medium containing MTX@LNP-PVCAM-1 or MTX@LNP at concentrations of 2.5 μg/mL, 5 μg/mL or 10 μg/mL. After an additional 24 hours of incubation, the supernatant was removed, and 100 μL of medium supplemented with 10% CCK-8 reagent was added to each well. The plates were then incubated for 2 hours at 37°C. Finally, the absorbance was measured at 450 nm using a microplate reader.

Cell Migration Test

The parallel migration ability of cells was evaluated using a scratch wound assay. MH7A cells were seeded into 6-well plates at a density of 8×10^3 cells/well and cultured in complete medium with or without 50 ng/mL TNF-α at 37°C with 5% CO_2. When the cells reached 90% confluence, a straight scratch was made perpendicular to the well using a 200 μL sterile pipette tip. Subsequently, the cells were treated with medium containing 10 μg/mL MTX@LNP-PVCAM-1 or MTX@LNP. Images of the scratched areas were captured and the scratch healing rate was quantitatively analyzed using ImageJ software.

The vertical migration ability of cells was assessed using a transwell assay. MH7A cell suspensions (5×10^4 cells in 200 μL) were seeded into the upper chamber. The upper chamber contained basal medium with 1% FBS, while the lower chamber was filled with complete medium containing 10% FBS and 50 ng/mL TNF-α as a chemoattractant. For the experimental groups, cells were pre-treated with medium containing 10 μg/mL MTX@LNP-PVCAM-1 or MTX@LNP 24 hours prior to seeding. The control group was treated with an equal volume of PBS. After 24 hours of incubation at 37°C with 5% CO_2, the migrated cells were fixed with 4% paraformaldehyde for 30 minutes and stained with 0.1% crystal violet for 15 minutes. The number of cells that migrated through the membrane was counted in five random fields under an upright optical microscope at ×200 magnification using ImageJ software.

Cellular Inflammatory Factor Inhibition Assay

MH7A cells were seeded into 24-well plates at a density of 5×10^4 cells/well and cultured in complete medium either containing 50 ng/mL TNF-α or TNF-α-free for 24 hours at 37°C. Subsequently, the culture medium was removed and replaced with fresh medium containing 10 μg/mL of MTX@LNP-PVCAM-1, or MTX@LNP. The cells were further incubated for an additional 24 hours. After incubation, the culture supernatant was collected by centrifugation, and inflammatory cytokine levels were measured using the Bio-Plex Pro™ Cytokine 23-Plex Assay Kit according to the manufacturer's instructions.

In vivo Imaging Studies in Rats

In vivo biodistribution and fluorescence imaging experiments were conducted using an antigen-induced arthritis (AIA) rat model. DIR-labeled formulations, including DIR@MTX@LNP-PVCAM-1, DIR@MTX@LNP, and free DIR dye, were administered via tail vein injection at a dose of 2 mg/kg. Fluorescence imaging was performed 6 hours post-injection using an IVIS Spectrum small-animal imaging system (PerkinElmer). 24 hours post-injection, rats were euthanized under isoflurane anesthesia. Tissues including the heart, liver, spleen, lungs, kidneys, and affected ankle joints were collected and placed on a black background for ex vivo fluorescence imaging. Then the fluorescence intensity was quantified using ImageJ software.

Pharmacodynamic Studies

To comprehensively evaluate the therapeutic efficacy of MTX@LNP-PVCAM-1 in AIA rats, a well-designed experimental protocol was implemented. On day 14 post-modeling, the successfully modeled rats were randomly divided into three groups (n=5 per group): Group 1 served as the control group and received an intravenous injection of saline. Groups 2 and 3 were administered MTX@LNP and MTX@LNP-PVCAM-1, respectively, both at a dose of 1.5 mg/kg. The treatment was administered intravenously every other day for a total of three doses. During the treatment period, the swelling of the rats' paws was photographed and the arthritis index was recorded. Additionally, the toe volume was measured using a plethysmometer to provide a quantitative assessment of edema.

Measurement of Inflammatory Factors

At the end of the treatment period, the AIA rats were euthanized, and soft tissues from the affected ankle joints were collected. The tissues were homogenized in PBS containing protease inhibitors and centrifuged to obtain the supernatant. The levels of IL-1β and IL-6 in the supernatant were quantified using ELISA kits according to the manufacturer's instructions.

X-Ray Joint Scan

Ankle joints from rats in each group were scanned using X-ray to evaluate structural changes in the ankle joints of AIA rats.

Micro CT Joint Scan

Ankle joints from rats in each group were scanned using Micro-CT to assess bone erosion, joint space and bone destruction.

Histological Assessment

Ankle joints from rats in each group were embedded in paraffin blocks, sectioned at 5 μm thickness, and stained with hematoxylin-eosin (H&E) for histological observation.

In vivo Safety Assessment

At the end of the experiment, blood samples were collected from the rats, and biochemical parameters were analyzed using an automated biochemical analyzer. Additionally, major organs from each group were harvested, fixed, and subjected to hematoxylin-eosin (H&E) staining to evaluate histopathological changes. These assessments provided insights into the therapeutic potential and safety profile of MTX@LNP-PVCAM-1 in vivo.

Statistical Analysis

The data were analyzed by SPSS13.0 software (SPSS, Chicago, IL, USA). The data were verified to meet the assumption of normality by the Shapiro–Wilk test. Significant differences were determined by *t*-test or one-way analysis of variance (ANOVA), and $p<0.05$ was considered statistically significant (GraphPad Prism 8 software, San Diego, CA, USA). In this study, post hoc multiple comparisons were performed using the Bonferroni method, which controls for categoryIerror rates by adjusting the significance level and is suitable for two-by-two comparisons between multiple groups.

Results

Characterization of MTX@LNP-PVCAM-1 and MTX@LNP

The particle size and zeta potential of MTX@LNP-PVCAM-1 and MTX@LNP were measured using dynamic light scattering (DLS). The results showed that the average particle size of MTX@LNP was 146.8 ± 4.1 nm, while that of MTX@LNP-PVCAM-1 was 168.5 ± 3.8 nm (Table 1, Figure 1a and b). The increase in particle size can be attributed to the modification of the nanoparticles by PVCAM-1. Additionally, PVCAM-1 was labeled with fluorescence, and the content of PVCAM-1 on the lipid nanoparticles was detected by fluorescence spectrophotometry. It was found that the content of PVCAM-1 on the lipid nanoparticles varied with different modification ratios (Figure S1). These findings further confirm that PVCAM-1 has been successfully modified on the surface of MTX@LNP, thereby forming the

Table 1 The Characterization of Lipid Nanoparticles

Lipid Nanoparticles	Size (nm)	Zeta (mV)	PDI	DL (%)	EE (%)
MTX@LNP-PVCAM-1	168.5±3.8	−12.1±1.7	0.142±0.08	24.3±3.7	64.3±8.9
MTX@LNP	146.5±4.1	−15.6±2.1	0.265±0.05	20.5±2.5	55.6±6.6

targeted lipid nanoparticles MTX@LNP-PVCAM-1. The surface potentials of MTX@LNP and MTX@LNP-PVCAM-1 were −15.6 ± 2.1 mV and −12.1 ± 1.7 mV, respectively. The weak electrostatic repulsion between nanoparticles enhances their dispersion and storage stability, preventing disintegration, precipitation, or phase separation. Transmission electron microscopy (TEM) images (Figures 1c and d, S2) showed that the nanoparticles exhibited uniform dispersion without adhesion, and their surface morphology was smooth and spherical.

Stability of Nanocarriers

The stability of MTX@LNP-PVCAM-1 and MTX@LNP was evaluated at different temperatures. When stored in PBS culture media at 4°C, both formulations showed minimal changes in particle size and polydispersity index (PDI) over seven days (Figures 1e and S3a). Similarly, when exposed to fetal bovine serum (FBS) culture media at 37°C, both formulations exhibited minimal changes in particle size and PDI over 24 hours (Figures 1f, S3b). These results indicate that the nanocarriers are stable under both storage and physiological conditions.

pH-Sensitive Drug Release

The pH of the microenvironment of inflamed tissues is significantly lower than that of normal tissues due to the hypoxic environment within the tissues and the excess lactic acid produced by inflammatory cells. This is important for biostimulation-mediated delivery of targeted drugs. Consequently, in this experiment, we prepared phosphate buffer solutions with different pH values (7.4, 6.0) to simulate the circulating pH and the weakly acidic pH of inflammatory cells at a temperature of 37°C (Table 2, Figure 1g and h). Under simulated physiological conditions (pH 7.4), the system exhibited sustained-release characteristics with approximately 30% drug release over 48 hours. In contrast, in an acidic microenvironment (pH 6.0), the cumulative drug release significantly increased to 80% (p<0.05). It is noteworthy that

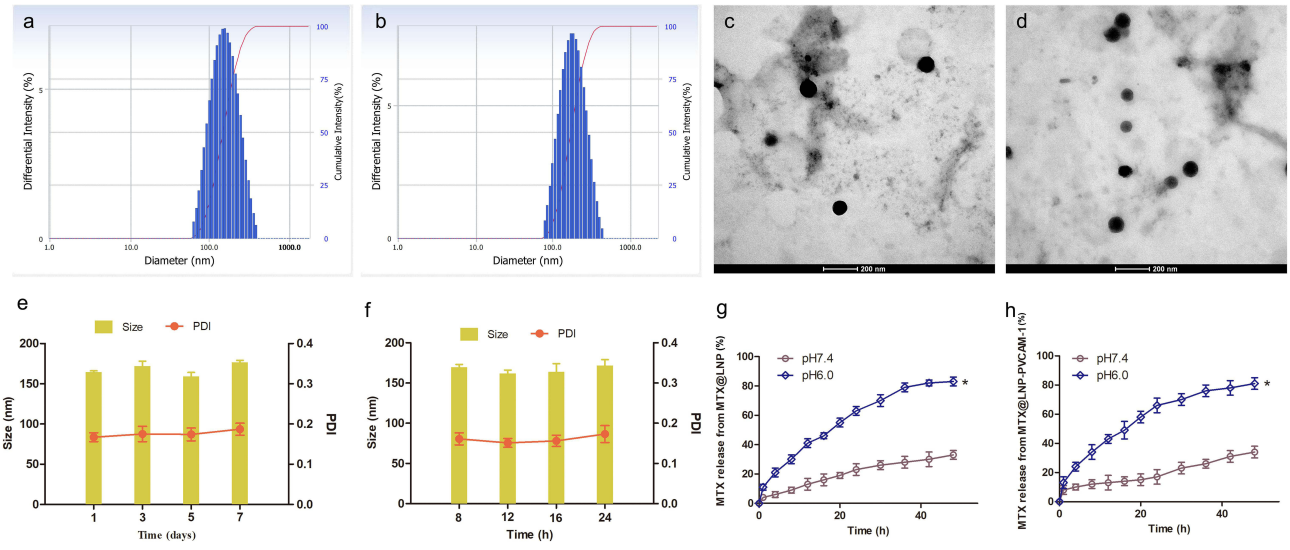

Figure 1 Characterization of MTX@LNP-PVCAM-1. Particle size distribution of (**a**) MTX@LNP and (**b**) MTX@LNP-PVCAM-1. TEM images of (**c**) MTX@LNP and (**d**) MTX@LNP-PVCAM-1. Stability of MTX@LNP-PVCAM-1 in (**e**) PBS and (**f**) FBS. In vitro MTX release from (**g**) MTX@LNP and (**h**) MTX@LNP-PVCAM-1 in different pH release medium. Data are presented as the mean ± SEM (n=3, *p<0.05 vs pH7.4).

Table 2 In vitro MTX Release from MTX@LNP and MTX@LNP-PVCAM-1 in Different pH Release Medium

Time (h)	MTX@LNP (pH7.4)	MTX@LNP (pH6.0)	MTX@LNP-PVCAM-1 (pH7.4)	MTX@LNP-PVCAM-1 (pH6.0)
0	0	0	0	0
1	4.1±0.5	11.3±0.7	8.2±0.4	13.8±0.8
4	5.2±0.4	21.3±1.6	10.3±0.9	24.3±1.2
8	7.1±0.8	30.5±1.9	12.7±0.8	34.7±2.7
12	9.4±1.5	41.6±2.8	13.7±0.5	43.5±2.9
16	11.2±0.9	46.5±3.6	14.3±0.7	49.1±3.1
20	13.5±0.5	51.1±2.1	15.2±1.1	58.2±4.2
24	15.2±1.5	59.2±3.2	17.5±1.7	66.2±4.6
30	21.7±2.2	68.4±4.3	23.6±1.5	70.5±3.6
36	25.3±3.4	74.7±4.7	26.1±2.6	76.3±3.5
42	30.8±3.5	76.6±3.5	31.4±3.1	78.4±3.8
48	33.2±4.1	79.4±3.9	34.2±2.4	81.8±5.1

similarly, the MTX@LNP system has also demonstrated pH-responsive drug release characteristics. This controlled release behavior highlights the flexibility and efficiency of nanocarriers in optimizing therapeutic outcomes.

Biocompatibility

The hemolytic potential of LNP-PVCAM-1 and LNP was evaluated by incubating them with erythrocytes at concentrations ranging from 250 μg/mL to 2000 μg/mL. The hemolysis rate remained below 5% at all tested concentrations, indicating no hemolytic activity (Figure 2a–c). Additionally, the cytotoxicity of blank lipid nanoparticles was assessed using a MTT assay with human umbilical vein endothelial cells (HUVEC). The cell survival rates remained above 90% across the entire concentration range, demonstrating minimal cytotoxicity (Figure 2d and e). These results collectively demonstrate that the prepared lipid nanoparticles, LNP-PVCAM-1 and LNP, exhibit favorable biocompatibility. This favorable biocompatibility profile provides a robust foundation for their application in both in vivo and in vitro delivery systems, paving the way for further research and potential clinical applications.

Targeting Ability

The targeting ability of PVCAM-1 to MH7A cells was thoroughly evaluated by analyzing the uptake of MTX@LNP-PVCAM-1 and MTX@LNP by both activated and unactivated MH7A cells. The results showed that, for unactivated MH7A cells, there was no significant difference in the uptake of MTX@LNP-PVCAM-1 and MTX@LNP (Figure 3a and b), indicating that the nanoparticles modified with PVCAM-1 did not exhibit additional targeting advantages in the unactivated state. However, for activated MH7A cells, the uptake of MTX@LNP-PVCAM-1 was significantly higher than that of MTX@LNP ($p<0.05$), which suggests that PVCAM-1 can significantly enhance the targeting of nanoparticles to activated MH7A cells (Figure 3a and c). In further experiments, after pre-treating activated MH7A cells with PVCAM-1, we found a significant decrease in the uptake of MTX@LNP-PVCAM-1 by the cells ($p<0.05$). This result further confirms the specific interaction between PVCAM-1 and the binding sites on the surface of activated MH7A cells, thereby verifying that PVCAM-1 has a highly specific targeting ability to activated MH7A cells.

Anti-Inflammatory and Anti-Proliferative Effects

The impact of MTX@LNP-PVCAM-1 on the proliferation of activated MH7A cells was further assessed using the MTT assay (Figure 4a). The results showed that, compared with the MTX@LNP group, MTX@LNP-PVCAM-1 significantly inhibited the proliferation of activated MH7A cells ($p<0.05$). The anti-inflammatory potential of MTX@LNP-PVCAM-1 was further elucidated using ELISA kits (Figure 4b and c). The data revealed that TNF-α stimulation significantly upregulated the expression of IL-6 and IL-1β in MH7A cells. Compared with the MTX@LNP group, MTX@LNP-PVCAM-1 could more efficiently suppress the levels of these two inflammatory cytokines, bringing them close to the normal range ($p<0.05$). In this study, MTX@LNP-PVCAM-1 not only significantly inhibited the proliferation of

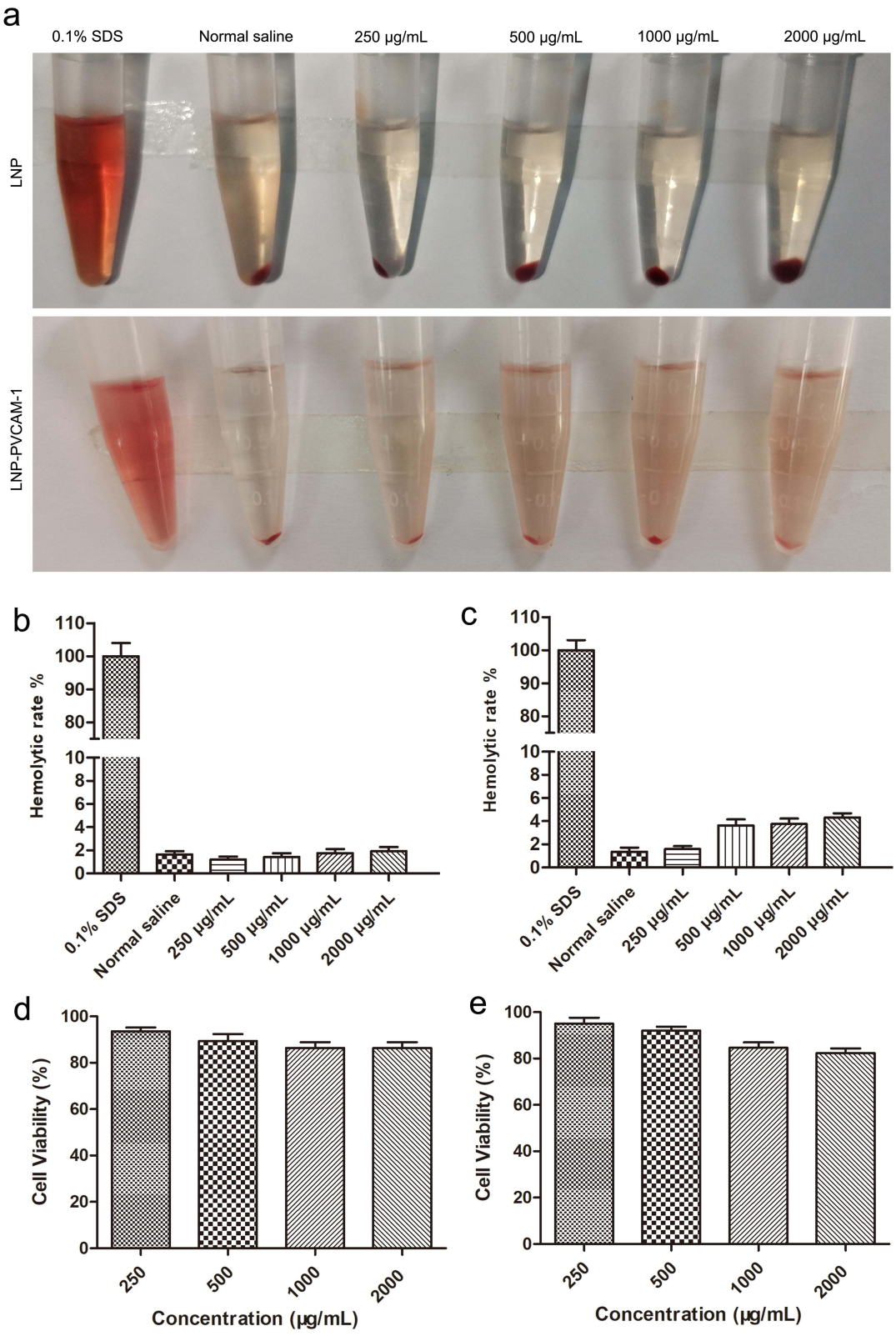

Figure 2 Bio-security of LNP-PVCAM-1. (**a**) Erythrocyte hemolysis of LNP and LNP-PVCAM-1. The hemolysis rate of (**b**) LNP and (**c**) LNP-PVCAM-1. CCK-8 assay to detect the cellular toxicity of (**d**) LNP and (**e**) LNP-PVCAM-1 on HUVEC cells. Data are presented as the mean ± SEM.

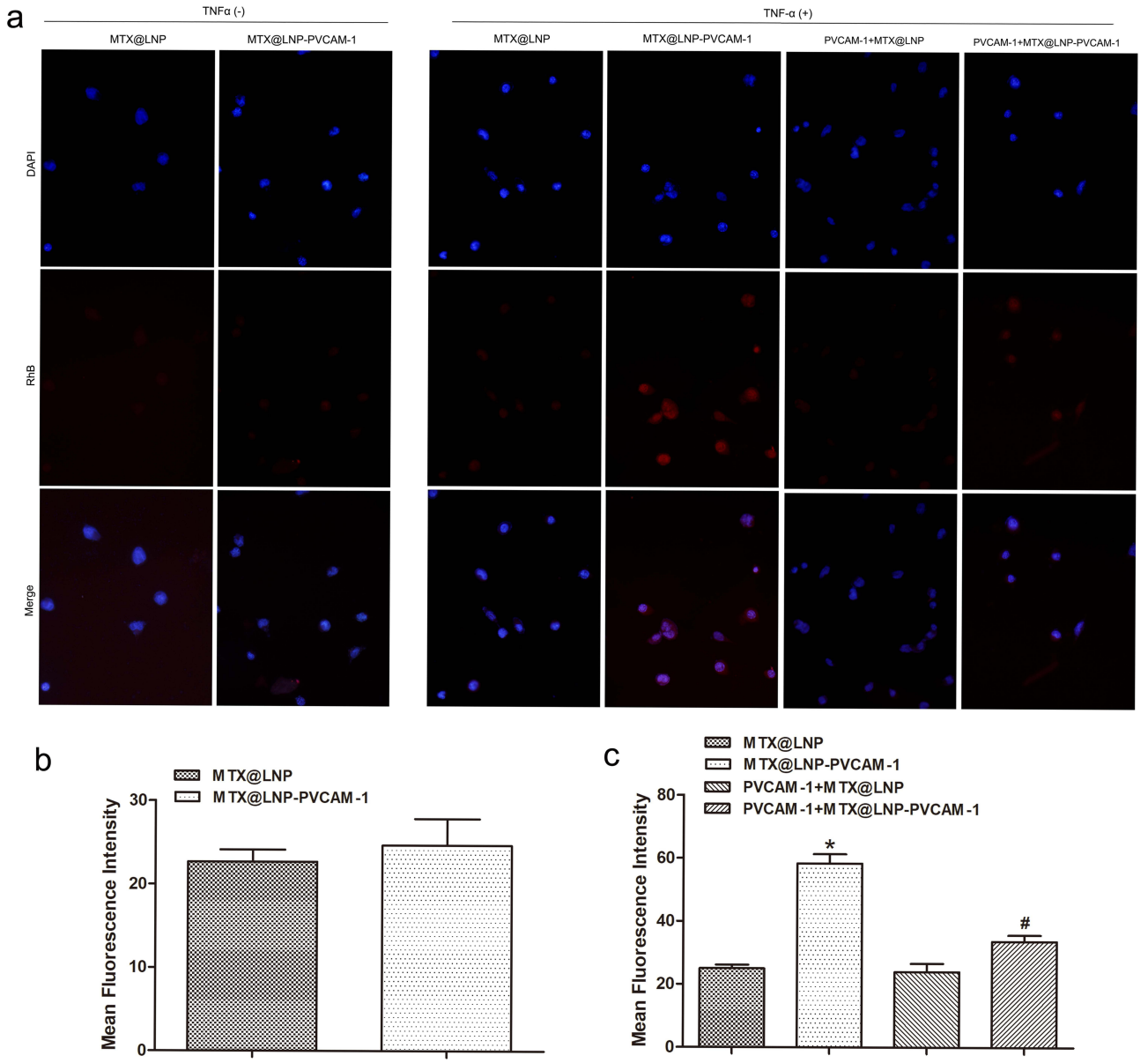

Figure 3 In vitro intracellular uptake after MTX@LNP-PVCAM-1 treatment. (**a**) Cellular uptake of MTX@LNP and MTX@LNP-PVCAM-1 in untreated and TNF-α activated MH7A cells, observed by CLSM. Semi-quantitative analysis results of MTX@LNP and MTX@LNP-PVCAM-1 in (**b**) untreated and (**c**) TNF-α activated MH7A cells. Data are presented as the mean ± SEM (n=3, $^{*}p<0.05$ vs MTX@LNP, $^{\#}p<0.05$ vs MTX@LNP-PVCAM-1).

activated MH7A cells but also robustly suppressed the production of inflammatory cytokines. These dual actions—reduced cytotoxicity and potent anti-inflammatory activity—jointly highlight the significant therapeutic advantages of MTX@LNP-PVCAM-1 in the treatment of RA.

Inhibition of Cell Migration

Targeted inhibition of HFLS-RA cell migration has emerged as a crucial therapeutic strategy to alleviate joint destruction. In this study, scratch wound healing assays and transwell migration experiments were employed to systematically evaluate the inhibitory effect of MTX@LNP-PVCAM-1 on TNF-α-induced horizontal and vertical migration of MH7A cells. Compared with the MTX@LNP group, treatment with MTX@LNP-PVCAM-1 significantly reduced the wound closure rate by 37.2% ($p<0.05$), indicating that PVCAM-1-modified nanoparticles markedly enhanced the inhibitory effect on horizontal cell migration (Figure 4d and f). The transwell assay results showed that, in comparison to the

https://doi.org/10.2147/IJN.S532163

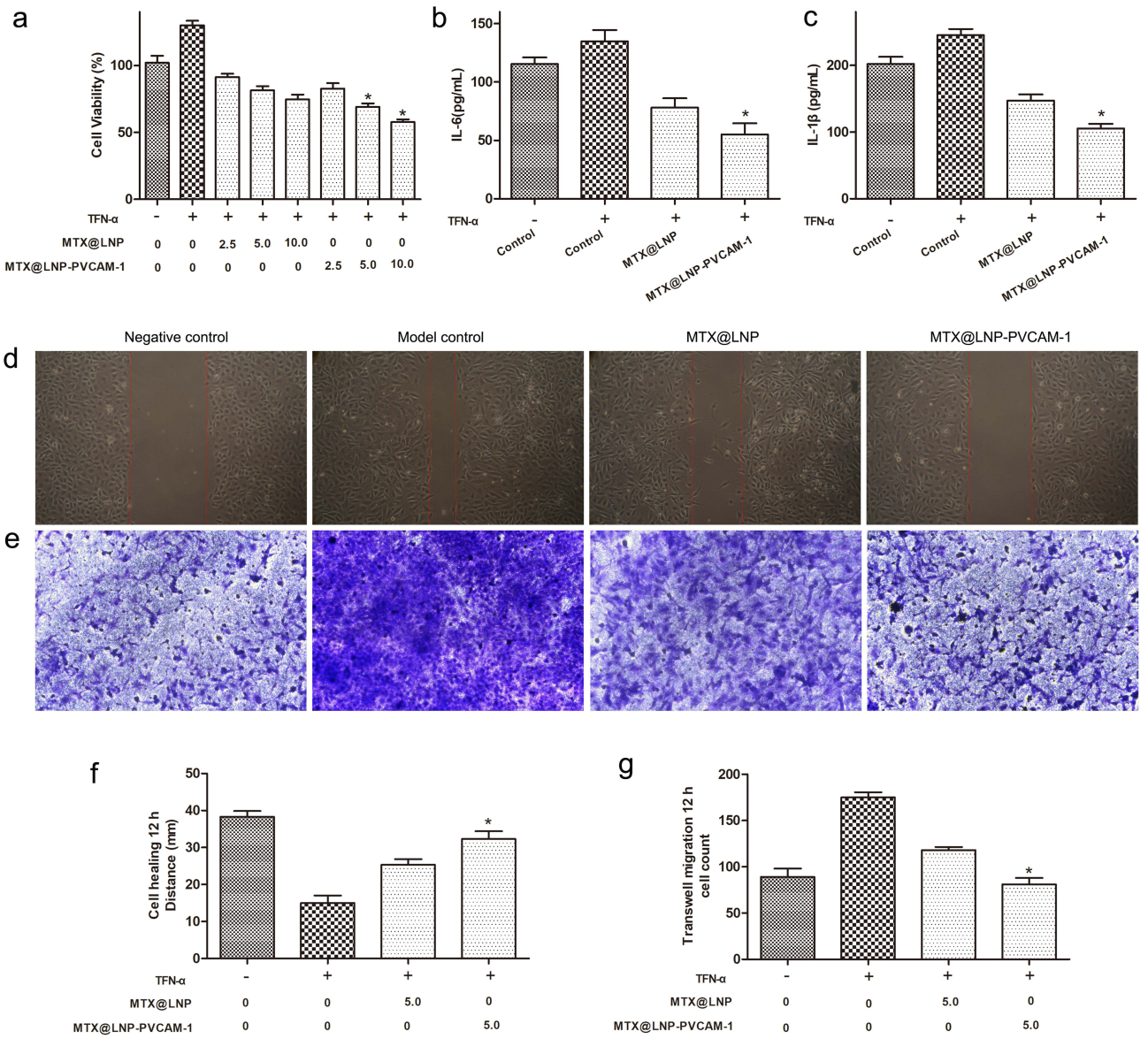

Figure 4 The effect of MTX@LNP-PVCAM-1 on cytotoxicity assessment, anti-inflammatory efficacy, and migratory behavior modulation of MH7A cells. (**a**) The effect of MTX@LNP-PVCAM-1 on cytotoxicity. (**b** and **c**) The effect of MTX@LNP-PVCAM-1 on anti-inflammatory efficacy. The effect of MTX@LNP-PVCAM-1 on migration was evaluated by (**d** and **f**) wound healing and (**e** and **g**) transwell assays. Data are presented as the mean ± SEM (n=3, *p<0.05 vs MTX@LNP).

MTX@LNP group, MTX@LNP-PVCAM-1 significantly decreased the number of cells migrating through the membrane in vertical migration by 52.8% (p<0.05) (Figure 4e and g). These findings demonstrate that PVCAM-1-modified nanoparticles, through targeted delivery, significantly enhance the inhibitory effect on HFLS-RA cell migration, both in terms of horizontal and vertical migration.

In vivo Targeting Efficacy

The in vivo targeting efficacy of MTX@LNP-PVCAM-1 was evaluated in adjuvant-induced arthritis (AIA) model rats using near-infrared fluorescent probe DIR-labeled nanoparticles. Free DIR exhibited minimal fluorescence signals in hindlimb joints, while both DIR-MTX@LNP and DIR-MTX@LNP-PVCAM-1 groups showed significant fluorescence accumulation at inflammatory joints within 6 hours (Figure 5a–d). The PVCAM-1-modified group exhibited higher fluorescence intensity at target sites compared to conventional nanoparticles (p<0.05), confirming enhanced active targeting.

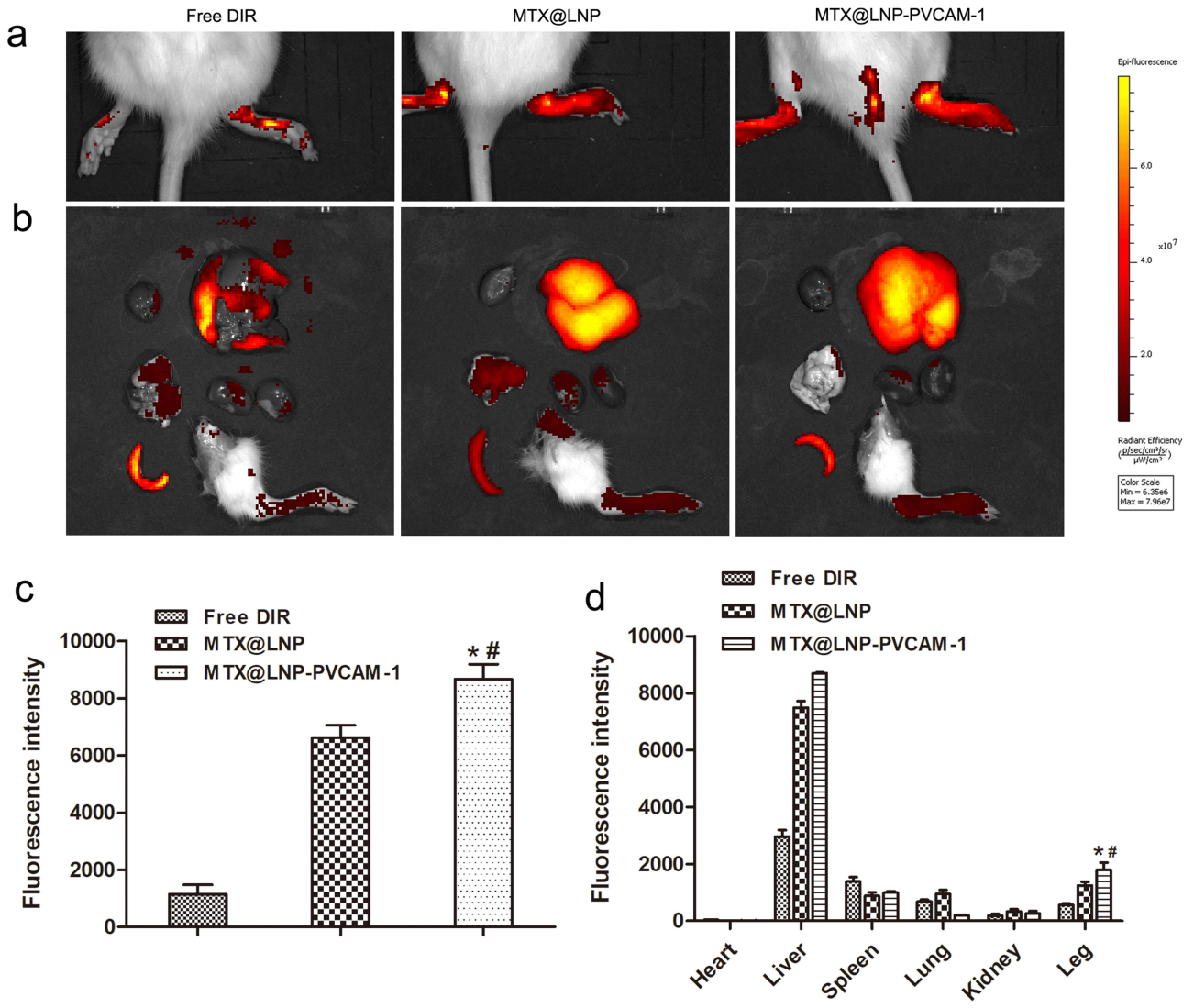

Figure 5 Biodistribution of MTX@LNP-PVCAM-1 in AIA rats. (**a**) In vivo images of the inflamed joints and (**b**) ex vivo images of the major organs from AIA rats after administration of different formulations. The fluorescent intensity (**c**) in the inflamed joints for 6 h in vivo and (**d**) in the major organs for 24 h Ex vivo from the fluorescence images. Data are presented as the mean ± SEM (n=3, *p<0.05 vs MTX@LNP, #p<0.05 vs Free DIR).

Therapeutic Efficacy in AIA Model Rats

The therapeutic efficacy of MTX@LNP-PVCAM-1 was evaluated in AIA model rats. The results showed that significant toe joint swelling was observed in the model group from day 14 post-modeling (Figure 6a). Compared with the model group, both MTX@LNP and MTX@LNP-PVCAM-1 significantly inhibited foot swelling and reduced arthritis index scores (p<0.05). Notably, MTX@LNP-PVCAM-1 exhibited superior therapeutic effects compared with MTX@LNP (p<0.05). At the end of the treatment, complete resolution of foot swelling was observed in the MTX@LNP-PVCAM-1 group (Figure 6b and c), indicating its significant advantage in alleviating joint swelling. Moreover, MTX@LNP-PVCAM-1 also showed a more pronounced effect in reducing the levels of IL-6 and IL-1β in rat joint homogenates compared with MTX@LNP (Figure 6d and e), further confirming its stronger anti-inflammatory potency. MTX@LNP-PVCAM-1 demonstrated significantly better therapeutic effects than MTX@LNP in AIA model rats, excelling not only in reducing joint swelling but also in lowering the levels of key inflammatory cytokines. These results indicate that the PVCAM-1 mediated targeted delivery strategy can significantly enhance the therapeutic efficacy of methotrexate.

https://doi.org/10.2147/IJN.S532163

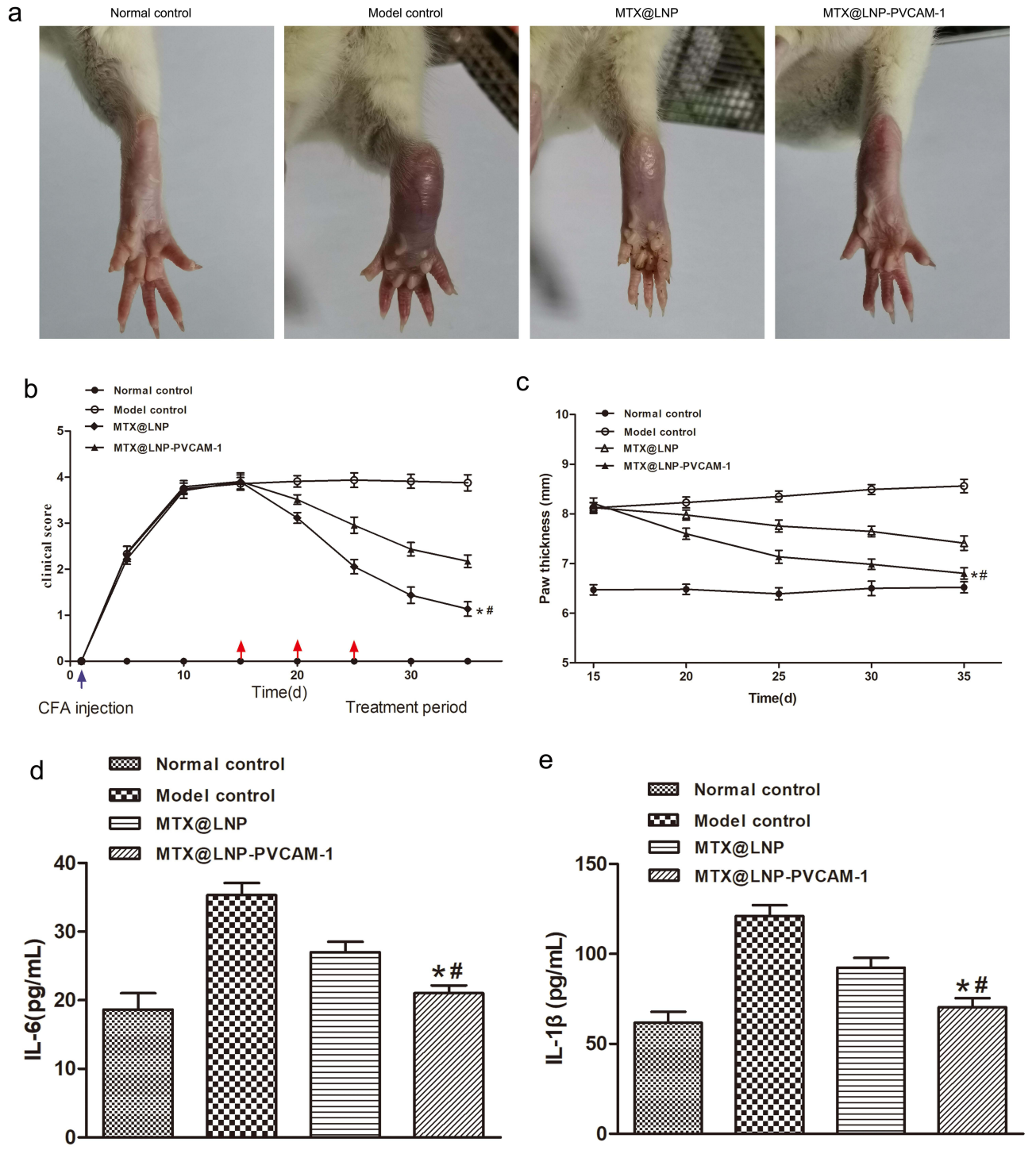

Figure 6 Effects of treatment on the clinical score, paw thickness, and pro-inflammatory cytokines. (**a**) Photographs of rat paws after treatment from different groups. (**b**) The clinical score and (**c**) paw thickness during the treatment. The levels of (**d**) IL-6 and (**e**) IL-1β in the joint tissue after the treatment. Data are presented as the mean ± SEM (n=3, *$p<0.05$ vs MTX@LNP, #$p<0.05$ vs Model control).

Histological and Imaging Analysis

H&E staining clearly revealed the significant effect of the MTX@LNP-PVCAM-1 group in improving joint pathology (Figure 7a). X-ray imaging further indicated that the joint structure in the MTX@LNP-PVCAM-1 group remained intact without obvious joint deformity, and both toe joint swelling and bone damage were significantly alleviated (Figure 7b). Micro-CT analysis provided strong evidence at the level of bone tissue structure: compared with the MTX@LNP group,

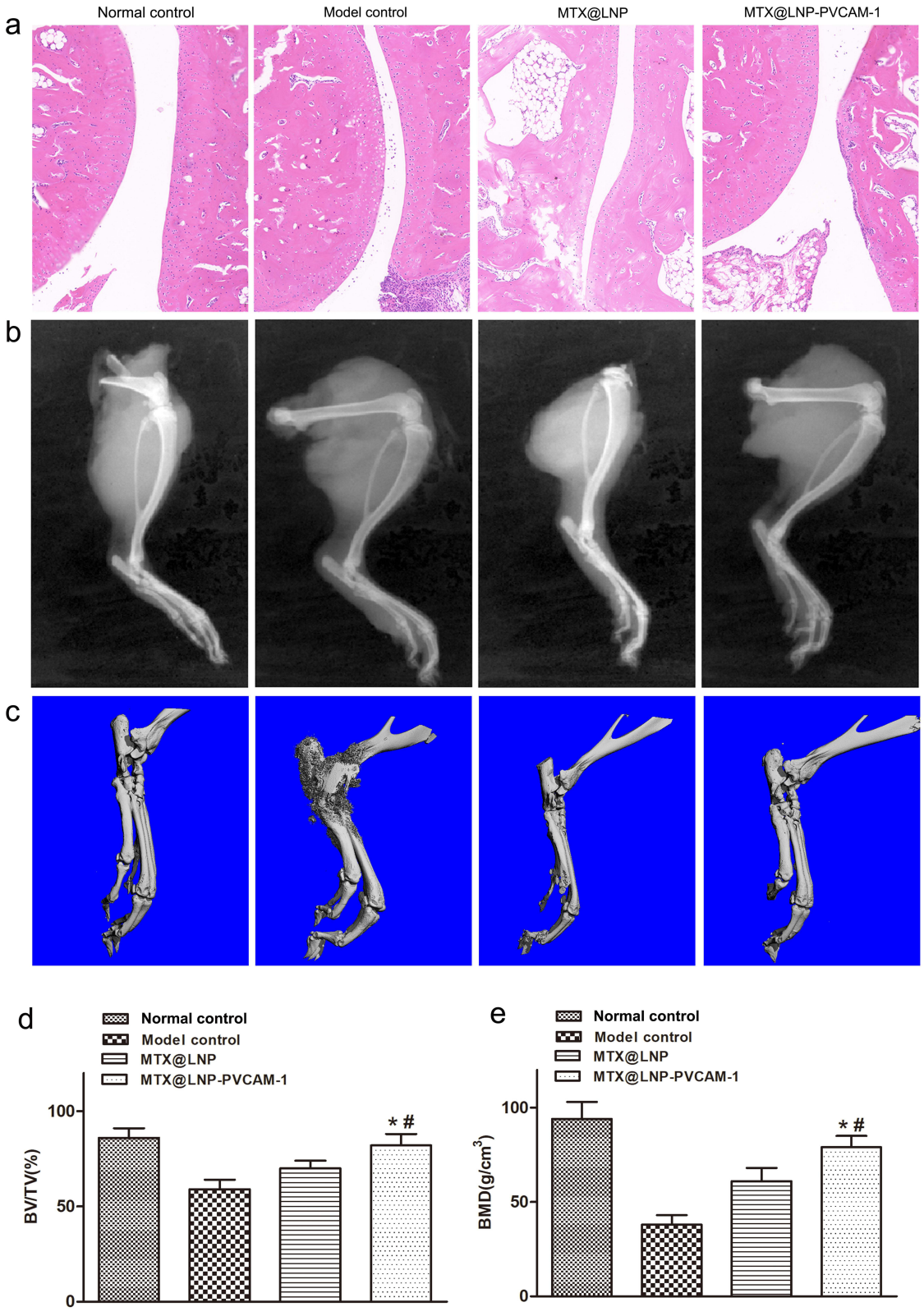

Figure 7 Evaluation of the therapeutic efficacy of different groups. (**a**) H&E, (**b**) X-ray evaluation, (**c**) Micro-CT evaluation of different groups in vivo. Scale bar: (**d**) 100 μm. BV/TV and (**e**) BMD of the ankle joints. Data are presented as the mean ± SEM (n=3, *p<0.05 vs MTX@LNP, $^{\#}p$<0.05 vs Model control).

https://doi.org/10.2147/IJN.S532163

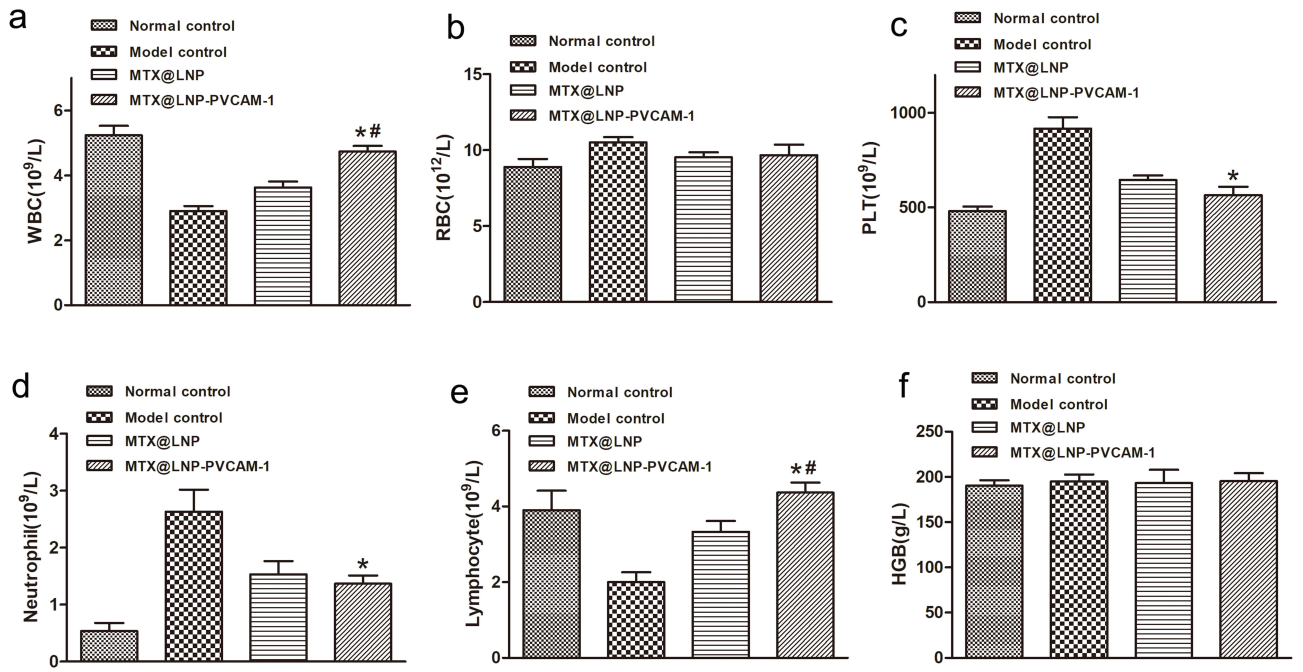

Figure 8 Hematological indices from different groups of rats. (**a**) WBC, (**b**) RBC, (**c**) PLT, (**d**) Neutrophil, (**e**) Lymphocyte, and (**f**) HGB levels in serum. Data are presented as the mean ± SEM (n=3, *p<0.05 vs MTX@LNP, #p<0.05 vs Model control).

rats treated with MTX@LNP-PVCAM-1 exhibited milder bone erosion, with significantly increased bone volume/tissue volume ratio (BV/TV) and bone mineral density (BMD), (p<0.05) (Figure 7c–e). MTX@LNP-PVCAM-1 has shown excellent therapeutic potential in reducing joint pathological changes, alleviating bone damage, and promoting bone tissue repair.

Analysis of Blood Routine Indicators in Rats

Blood routine test results in rats are shown in Figure 8. The white blood cell (WBC) count was lower in the model control group than in the normal control. The MTX@LNP-PVCAM-1 group significantly increased WBC levels compared to the MTX@LNP group (p<0.05), suggesting efficacy in restoring WBC count. Platelet (PLT) counts were higher in the model group than in the normal group. MTX@LNP-PVCAM-1 reduced PLT to near-normal levels, demonstrating its ability to correct abnormal platelet elevation. Model group neutrophil counts exceeded normal levels. MTX@LNP-PVCAM-1 significantly reduced neutrophil numbers, indicating regulatory effects on inflammation-associated neutrophils and alleviation of inflammation. Lymphocyte counts were lower in the model group than in normal controls. MTX@LNP-PVCAM-1 elevated lymphocyte levels and differed significantly from the MTX@LNP group (p<0.05), demonstrating capacity to modulate lymphocytes and restore immune balance. Red blood cell counts and hemoglobin (HGB) levels showed no significant differences between treatment groups and normal controls, indicating prolonged in vivo circulation does not affect blood cell counts and confirming excellent hemocompatibility. MTX@LNP-PVCAM-1 improved WBC, PLT, neutrophil, and lymphocyte parameters in rheumatoid arthritis (RA) rats, facilitating restoration of immune and blood-related functions. However, specific molecular mechanisms and long-term efficacy require further investigation through inflammatory cytokine detection and joint pathology analysis.

Safety and Biocompatibility

Biochemical analyses revealed no significant differences in hepatic function markers (ALT and AST) or renal function parameters (Cr and BUN) among experimental groups, confirming the absence of drug-induced hepatotoxicity and nephrotoxicity (Figure 9a–d). Histopathological analysis showed intact histological architecture of major organs in treated animals, with no inflammatory infiltration or necrotic lesions (Figure 9e).

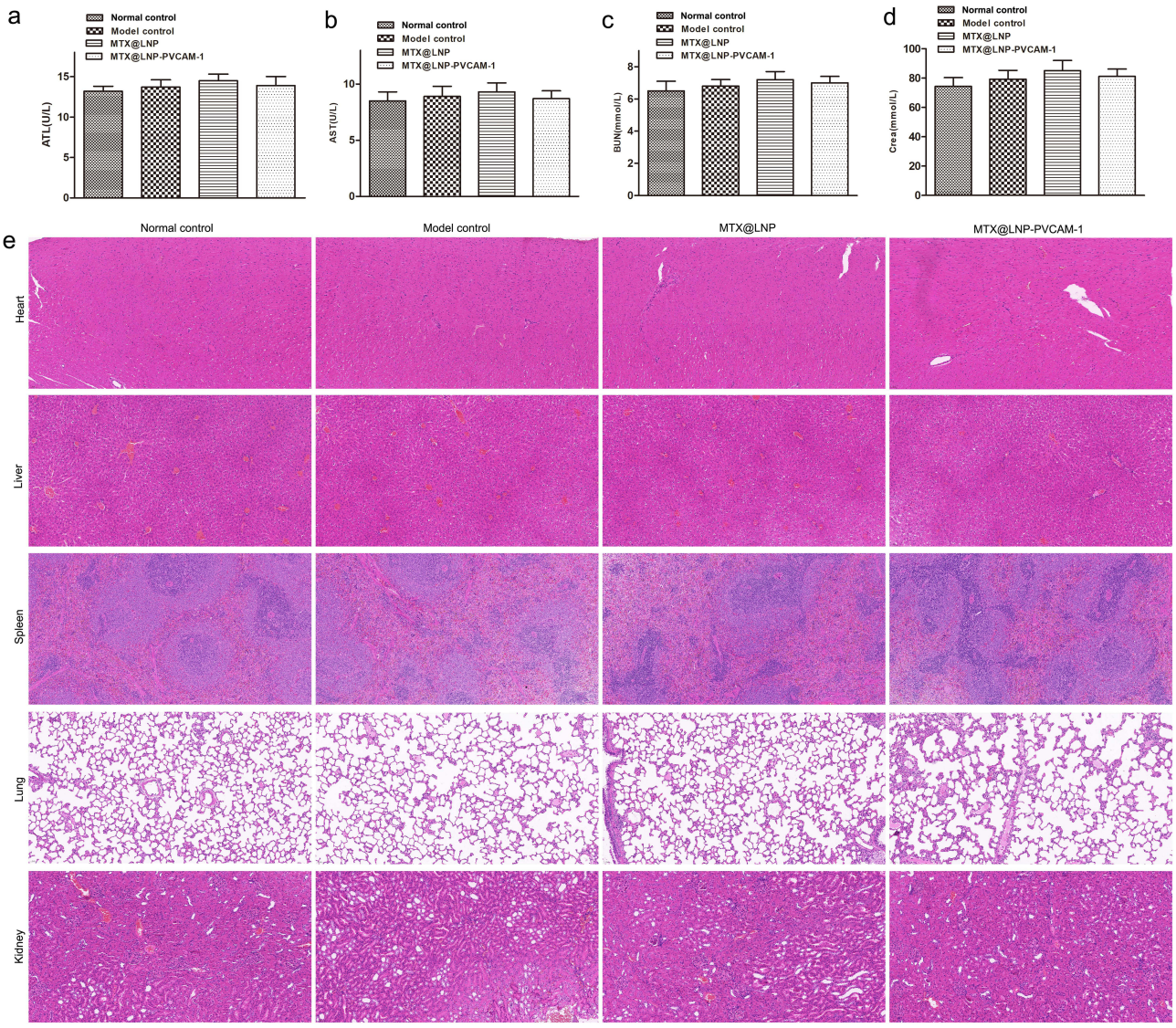

Figure 9 In vivo biocompatibility of MTX@LNP-PVCAM-1. (**a**) ALT, (**b**) AST, (**c**) BUN, and (**d**) Crea levels in serum. (**e**) H&E staining of major organs collected from different groups of rats.

Discussion

Physicochemical Properties and Stability

The physicochemical properties of nanocarriers are crucial for their delivery efficiency and biological activity. In this study, the average particle sizes of MTX@LNP and MTX@LNP-PVCAM-1 were 146.8 ± 4.1 nm and 168.5 ± 3.8 nm, respectively, falling within the ideal nanoscale range of 100–200 nm. This size range is optimal for the enhanced permeability and retention (EPR) effect, allowing passive targeting and accumulation at the lesion site.[27,28] Additionally, this size helps evade rapid clearance by the reticuloendothelial system (RES), thereby extending circulation time in the body.[29,30] The slight increase in particle size after PVCAM-1 modification (approximately 21.7 nm) is likely due to the grafting of PVCAM-1 molecules on the LNP surface, which is consistent with the general rule of size increase after surface functionalization.[31,32] This increase did not exceed the optimal size range for nanocarriers, ensuring their feasibility for in vivo delivery.

The zeta potential measurements revealed weak negative charges on the surfaces of both nanoparticles (−12.1 to −15 mV). This weak electrostatic repulsion effectively prevents particle aggregation, maintaining dispersion stability,[33] which

https://doi.org/10.2147/IJN.S532163

is consistent with the TEM observations of uniform dispersion without adhesion. The slight decrease in zeta potential absolute value after PVCAM-1 modification (from −15 mV to −12.1 mV) may be attributed to the neutralization of surface negative charges by polar groups in PVCAM-1 molecules. However, this did not compromise the overall dispersibility and may improve biocompatibility by reducing non-specific adsorption.

The stability experiments further confirmed that both nanocarriers exhibited minimal changes in particle size and PDI over 7 days at 4°C and 24 hours at 37°C in serum. This stability is critical: the low-temperature stability ensures long-term storage and transportation, while the physiological temperature stability in serum indicates that the nanocarriers are unlikely to disintegrate or aggregate during circulation, preventing premature drug leakage or clearance.[34] This stability is essential for subsequent targeting delivery and controlled release.

pH-Sensitive Drug Release

MTX@LNP-PVCAM-1 demonstrated significant pH-sensitive drug release characteristics. Under physiological conditions (pH 7.4), the drug release rate was approximately 30% over 48 hours, while in an acidic environment (pH 6.0), the release rate increased to 80%. This release profile is highly compatible with the microenvironment of RA lesions, where the pH is typically lower (approximately 6.0–6.5) due to inflammatory cell infiltration and high metabolic activity.[35] This "site-specific release" mode allows for precise drug release at the target site, significantly reducing drug exposure in normal tissues and thereby minimizing the systemic toxicity of MTX.

Mechanistically, the pH-dependent release behavior of MTX from the nanoparticles can be attributed to the protonation of MTX molecules within the aqueous core or at the interface of the nanoparticles 1–3. Upon protonation, MTX forms a more lipophilic neutral species (MTXH). This lipophilic MTXH can relatively easily diffuse through the hydrophobic lipid bilayer of the LNP to reach the external medium. Once MTXH enters the external environment near physiological pH (7.4), its carboxyl group rapidly undergoes deprotonation, reverting back to its highly hydrophilic and charged ionic form (MTX^-). The ionized MTX^- is extremely difficult to re-diffuse back into the hydrophobic lipid membrane. This leads to continuous accumulation of MTX^- in the external medium, disrupting the dynamic equilibrium across the membrane. Consequently, this drives the continuous diffusion and transformation of protonated MTXH from the interior, resulting in a significantly accelerated net release rate under acidic conditions.[36,37] Moreover, the sustained release under physiological conditions (30%/48 hours) avoids burst release and local toxicity, while the efficient release at the lesion site (80%/48 hours) ensures sufficient drug concentration for therapeutic effects, embodying the "on-demand release" concept for intelligent treatment.

Targeting Ability and Enhanced Therapeutic Efficacy

Targeted delivery is key to improving the specificity of RA treatment. In this study, PVCAM-1 modification significantly enhanced the targeting ability of the nanoparticles to activated MH7A cells. The uptake of MTX@LNP-PVCAM-1 by activated MH7A cells was significantly higher than that of unmodified MTX@LNP, and pre-treatment with PVCAM-1 blocked this uptake, confirming the specificity of the targeting. This targeting ability is closely related to the pathological features of RA, where synovial fibroblasts (eg, MH7A) express high levels of VCAM-1 upon activation by inflammatory cytokines (eg, TNF-α).[38] PVCAM-1 can specifically bind to VCAM-1 on the target cell surface, mediating active targeting and internalization of the nanoparticles, thereby increasing drug accumulation at the lesion site.

In vivo imaging results further validated this targeting advantage. DIR-labeled MTX@LNP-PVCAM-1 exhibited significantly higher fluorescence intensity at inflamed joints in AIA model rats compared to unmodified nanoparticles, while free DIR showed minimal accumulation. This indicates that PVCAM-1 modification enhances selective accumulation of the nanoparticles at the lesion site through a dual mechanism of "active targeting + EPR-mediated passive enrichment", laying the foundation for enhanced local therapeutic effects.

In vitro and In vivo Therapeutic Efficacy and Safety

In vitro functional experiments showed that MTX@LNP-PVCAM-1 significantly inhibited the proliferation of activated MH7A cells and effectively reduced levels of key inflammatory cytokines IL-6 and IL-1β. IL-6 and IL-1β are central pro-inflammatory cytokines in RA pathogenesis, driving synovial cell proliferation, osteoclast activation, and joint damage.[39,40]

Their reduced levels directly reflect the anti-inflammatory activity of the nanocarriers. Additionally, MTX@LNP-PVCAM-1 significantly inhibited TNF-α-induced migration of MH7A cells (reducing scratch wound healing by 37.2% and transwell migration by 52.8%), suggesting that it can slow down joint cartilage and bone destruction by inhibiting synovial cell invasion and migration.

In vivo therapeutic experiments further confirmed the superiority of MTX@LNP-PVCAM-1. In AIA model rats, this targeted nanocarrier completely resolved foot swelling, significantly reduced arthritis index scores, and decreased levels of IL-6 and IL-1β in joint homogenates. Histological and imaging analyses showed that it improved joint inflammation, reduced bone erosion, and increased bone volume/tissue volume (BV/TV) and bone mineral density (BMD). These results are consistent with in vitro findings, confirming that PVCAM-1-mediated targeting increases drug concentration at the lesion site, thereby enhancing the anti-inflammatory, anti-proliferative, and anti-migratory effects of MTX and ultimately improving joint structural damage.[41,42]

Safety assessment is a core prerequisite for the translational application of nanocarriers. In this study, LNP-PVCAM-1 and LNP exhibited no significant hemolytic activity at concentrations ranging from 250 to 2000 μg/mL and maintained cell viability above 90% in HUVEC cells, indicating good blood compatibility and cell compatibility.[43–45] In vivo experiments further confirmed that liver function (ALT, AST) and kidney function (Cr, BUN) indicators were normal in all treatment groups, and no inflammatory infiltration or necrosis was observed in major organs. This suggests that the nanocarriers can effectively reduce the systemic toxicity of free MTX, which is particularly important for clinical applications. Traditional MTX often causes liver, kidney, and hematological toxicity due to non-specific distribution,[46,47] while targeted nanocarriers reduce drug exposure in normal tissues, potentially improving the therapeutic window.

Significance and Limitations

The MTX@LNP-PVCAM-1 nanocarrier system integrates multiple advantages: active targeting through PVCAM-1, pH-sensitive release for precise control, enhanced therapeutic efficacy, and reduced systemic toxicity. These features make it a promising candidate for the precise treatment of RA. However, this study has certain limitations. First, the specific molecular mechanisms of PVCAM-1 interaction with VCAM-1 on target cells need further validation through receptor-blocking experiments or gene knockout models. Second, long-term (beyond 4 weeks) in vivo safety and efficacy have not been evaluated and should be confirmed in larger animal models. Finally, pharmacokinetic parameters (eg, half-life, clearance rate) of the nanoparticles and their combination with other RA treatments require further investigation.

Conclusion

The rationally engineered MTX@LNP-PVCAM-1 system demonstrates multifunctional superiority as a nano-therapeutic platform for RA management. Its uniform particle size, high drug-loading capacity, and stimuli-responsive release kinetics ensure precise spatiotemporal control of methotrexate delivery, while robust stability guarantees translational feasibility. In terms of clinical relevance, this system addresses MTX's current drawbacks in practice: by enhancing targeted accumulation at inflamed sites, it mitigates the systemic toxicity associated with high-dose MTX administration; the stimuli-responsive release profile reduces off-target effects, overcoming the narrow therapeutic window of free MTX; and the nanoformulation improves bioavailability, addressing issues of variable absorption in oral administration.

In vitro and in vivo investigations collectively validate its dual-action therapeutic mechanism: (1) Targeted accumulation at inflamed joints enables selective suppression of fibroblast-like synoviocyte proliferation and pro-inflammatory cytokine secretion, effectively interrupting the self-perpetuating inflammatory cascade; (2) Systemic protection against cartilage degradation and bone erosion is achieved through marked reduction of paw swelling, arthritis index scores, and inflammatory cell infiltration in AIA models. Crucially, comprehensive safety evaluations reveal no detectable hematological, hepatic, or renal toxicity, underscoring its exceptional biocompatibility. Regarding future steps, long-term toxicity studies and exploration of combination therapies (eg, with biologics) will be essential to further validate its translational potential, ensuring sustained safety and synergistic efficacy in chronic RA management. In terms of broader

implications, the platform's reliance on VCAM-1 targeting suggests potential applicability to other inflammatory diseases with VCAM-1 overexpression, such as inflammatory bowel disease or atherosclerosis, expanding its therapeutic scope beyond RA.

In summary, MTX@LNP-PVCAM-1 has the potential to be a promising therapeutic agent for the treatment of RA.

Data Sharing Statement

The raw data and processed data required to reproduce these findings are available from the corresponding author upon request.

Ethical Approval Statement

All procedures involving laboratory animals are performed in accordance with the ethics committee guidelines at the Fourth Military Medical University (ethical approval number: IACUC: 20230328).

Acknowledgment

This research was funded by the School of Pharmacy-Xijing Hospital, Fourth Military Medical University (LHJJ2023-YX07), Liaoning Province science and technology plan joint plan (2023JH2/101700113), Natural Science Foundation Program of Liaoning Province (2024-MS-249) and Shaanxi Province social development research project (2024SF-YBXM-410).

Author Contributions

All authors made a significant contribution to the work reported, whether that is in the conception, study design, execution, acquisition of data, analysis and interpretation, or in all these areas; took part in drafting, revising or critically reviewing the article; gave final approval of the version to be published; have agreed on the journal to which the article has been submitted; and agree to be accountable for all aspects of the work.

Disclosure

The authors declare that they have no known competing financial interests or personal relationships that could have appeared to influence the work reported in this paper.

References

1. Angstrom L, Hornberg K, Sundstrom B, Sodergren A. Rheumatoid cachexia in early rheumatoid arthritis: prevalence and associated variables. *Scand J Rheumatol*. 2023;52(1):10–16. doi:10.1080/03009742.2021.1973678
2. Morse JL, Afari N, Norman SB, Guma M, Pietrzak RH. Prevalence, characteristics, and health burden of rheumatoid arthritis in the U.S. veteran population. *J Psychiatr Res*. 2023;159:224–229. doi:10.1016/j.jpsychires.2023.01.039
3. Heinlen L, Humphrey MB. Skeletal complications of rheumatoid arthritis. *Osteoporos Int*. 2017;28(10):2801–2812. doi:10.1007/s00198-017-4170-5
4. Jin H, Wang G, Lu Q, et al. Pathophysiology of myopenia in rheumatoid arthritis. *Bone Res*. 2025;13(1):64. doi:10.1038/s41413-025-00438-9
5. Sanghavi N, Ingrassia JP, Korem S, Ash J, Pan S, Wasserman A. Cardiovascular manifestations in rheumatoid arthritis. *CARDIOL REV*. 2024;32(2):146–152. doi:10.1097/CRD.0000000000000486
6. Liu X, Zhang G, Liu L, Xiong G, Liu J, Wei W. Usp2 promotes the proliferation and inflammation of fibroblast-like synovial cells in rheumatoid arthritis through deubiquitination of Traf2. *Biochem Genet*. 2025;63(1):592–605. doi:10.1007/s10528-024-10737-1
7. Zhu J, Lin Y, Li G, et al. Dual-targeted halofuginone hydrobromide nanocomplexes for promotion of macrophage repolarization and apoptosis of rheumatoid arthritis fibroblast-like synoviocytes in adjuvant-induced arthritis in rats. *J Pharm AnaL*. 2024;14(11):100981. doi:10.1016/j.jpha.2024.100981
8. Gao Y, Zhang Y, Liu X. Rheumatoid arthritis: pathogenesis and therapeutic advances. *Medcomm*. 2024;5(3):e509. doi:10.1002/mco2.509
9. Piantoni S, Ohrndorf S. Editorial: rheumatoid Arthritis: Pathogenesis And Target-Treatments. *Front Med-Lausanne*. 2023;10:1145163. doi:10.3389/fmed.2023.1145163
10. Qi P, Chen X, Tian J, et al. The gut homeostasis-immune system axis: novel insights into rheumatoid arthritis pathogenesis and treatment. *Front Immunol*. 2024;15:1482214. doi:10.3389/fimmu.2024.1482214
11. Zhao Z, Hua Z, Luo X, et al. Application and pharmacological mechanism of methotrexate in rheumatoid arthritis. *Biomed Pharmacother*. 2022;150:113074. doi:10.1016/j.biopha.2022.113074
12. Torres RP, Santos FP, Branco JC. Methotrexate: implications of pharmacogenetics in the treatment of patients with rheumatoid arthritis. *ARP Rheumatol*. 2022;1(3):225–229.
13. Wang W, Zhou H, Liu L. Side effects of methotrexate therapy for rheumatoid arthritis: a systematic review. *Eur J Med Chem*. 2018;158:502–516.

14. Guo P, Huang C, Yang Q, et al. Advances in formulations of microneedle system for rheumatoid arthritis treatment. *Int J Nanomed*. 2023;18:7759–7784. doi:10.2147/IJN.S435251
15. Jeong M, Park JH. Nanomedicine for the treatment of rheumatoid arthritis. *Mol Pharm*. 2021;18(2):539–549. doi:10.1021/acs.molpharmaceut.0c00295
16. Prasad P, Verma S, Surbhi Ganguly NK, Chaturvedi V, Mittal SA, Mittal SA. Rheumatoid arthritis: advances in treatment strategies. *Mol Cell Biochem*. 2023;478(1):69–88. doi:10.1007/s11010-022-04492-3
17. Cao S, Zhang W, Pan H, et al. Bioactive lipid-nanoparticles with inherent self-therapeutic and anti-angiogenic properties for cancer therapy. *Acta biomater*. 2023;157:500–510. doi:10.1016/j.actbio.2022.12.022
18. Musielak E, Feliczak-Guzik A, Nowak I. Synthesis and potential applications of lipid nanoparticles in medicine. *Materials*. 2022;15(2):682. doi:10.3390/ma15020682
19. Achudhan D, Li-Yun CS, Liu SC, et al. Antcin K inhibits vcam-1-dependent monocyte adhesion in human rheumatoid arthritis synovial fibroblasts. *Food Nutr Res*. 2022;66. doi:10.29219/fnr.v66.8645
20. Chi PL, Chuang YC, Chen YW, Lin CC, Hsiao LD, Yang CM. The co donor corm-2 inhibits Lps-induced vascular cell adhesion molecule-1 expression and leukocyte adhesion in human rheumatoid synovial fibroblasts. *Brit J Pharmacol*. 2014;171(12):2993–3009. doi:10.1111/bph.12680
21. Zhang C, Huang W, Huang C, et al. Vhpkqhr peptide modified ultrasmall paramagnetic iron oxide nanoparticles targeting rheumatoid arthritis for T (1)-weighted magnetic resonance imaging. *Front Bioeng Biotech*. 2022;10:821256. doi:10.3389/fbioe.2022.821256
22. Rafik ST, Zeitoun TM, Shalaby TI, Barakat MK, Ismail CA. Methotrexate conjugated gold nanoparticles improve rheumatoid vascular dysfunction in rat adjuvant-induced arthritis: gold revival. *Inflammopharmacology*. 2023;31(1):321–335. doi:10.1007/s10787-022-01104-w
23. Szeremeta A, Jura-Poltorak A, Zon-Giebel A, Olczyk K, Komosinska-Vassev K. Tnf-alpha inhibitors in combination with Mtx reduce circulating levels of heparan sulfate/heparin and endothelial dysfunction biomarkers (sVCAM-1, MCP-1, MMP-9 and ADMA) in women with rheumatoid arthritis. *J Clin Med*. 2022;11:14. doi:10.3390/jcm11144213
24. Patra S, Dey J, Chakraborty A. Physicochemical characterization, stability, and in vitro evaluation of curcumin-loaded solid lipid nanoparticles prepared using biocompatible synthetic lipids. *Acs Appl Bio Mater*. 2023;6(7):2785–2794. doi:10.1021/acsabm.3c00252
25. Zoller K, Haddadzadegan S, Lindner S, Veider F, Bernkop-Schnurch A. Design of charge converting lipid nanoparticles via a microfluidic coating technique. *Drug Deliv Transl Re*. 2024;14(11):3173–3185. doi:10.1007/s13346-024-01538-5
26. Marques SS, Ramos II, Fernandes SR, et al. Insights on ultrafiltration-based separation for the purification and quantification of methotrexate in nanocarriers. *Molecules*. 2020;25:8. doi:10.3390/molecules25081879
27. Ferreira-Silva M, Faria-Silva C, Baptista PV, Fernandes E, Fernandes AR, Corvo ML. Drug delivery nanosystems targeted to hepatic ischemia and reperfusion injury. *Drug Deliv Transl Re*. 2021;11(2):397–410. doi:10.1007/s13346-021-00915-8
28. Qiao Q, Liu X, Yang T, et al. Nanomedicine for acute respiratory distress syndrome: the latest application, targeting strategy, and rational design. *Acta Pharm Sin B*. 2021;11(10):3060–3091. doi:10.1016/j.apsb.2021.04.023
29. Jadhav D, Vavia P. Dexamethasone sodium phosphate loaded modified cyclodextrin based nanoparticles: an efficient treatment for rheumatoid arthritis. *J Pharm Sci-US*. 2021;110(3):1206–1218. doi:10.1016/j.xphs.2020.10.023
30. Tian J, Chen T, Huang B, et al. Inflammation specific environment activated methotrexate-loaded nanomedicine to treat rheumatoid arthritis by immune environment reconstruction. *Acta Biomater*. 2023;157:367–380. doi:10.1016/j.actbio.2022.12.007
31. Kim M, Lee JS, Kim W, et al. Aptamer-conjugated nano-liposome for immunogenic chemotherapy with reversal of Immunosuppression. *J Control Release*. 2022;348:893–910. doi:10.1016/j.jconrel.2022.06.039
32. Liu B, Yang W, Che C, et al. A targeted nano drug delivery system of as1411 functionalized graphene oxide based composites. *Chemistryopen*. 2021;10(4):408–413. doi:10.1002/open.202000226
33. Liu S, Wen Y, Shan X, et al. Charge-assisted stabilization of lipid nanoparticles enables inhaled mrna delivery for mucosal vaccination. *Nat Commun*. 2024;15(1):9471. doi:10.1038/s41467-024-53914-x
34. Mahajan K, Bhattacharya S. The advancement and obstacles in improving the stability of nanocarriers for precision drug delivery in the field of nanomedicine. *Curr Top Med Chem*. 2024;24(8):686–721. doi:10.2174/0115680266287101240214071718
35. Lin Y, Tang Y, Yi O, et al. Graphene oxide quantum dots-loaded sinomenine hydrochloride nanocomplexes for effective treatment of rheumatoid arthritis via inducing macrophage repolarization and arresting abnormal proliferation of fibroblast-like synoviocytes. *J Nanobiotechnol*. 2024;22(1):383. doi:10.1186/s12951-024-02645-8
36. Agafonov M, Ivanov S, Terekhova I. Improvement of pharmacologically relevant properties of methotrexate by solid dispersion with pluronic F127. *Mat Sci Eng C-Mater*. 2021;124:112059. doi:10.1016/j.msec.2021.112059
37. Kumar M, Kumar R, Singh P, Sharma B, Katare G, Raza OP. In vivo pharmacokinetic studies and intracellular delivery of methotrexate by means of glycine-tethered plga-based polymeric micelles. *Int J Pharmaceut*. 2017;519(1–2):138–144. doi:10.1016/j.ijpharm.2017.01.021
38. Voicu G, Mocanu CA, Safciuc F, et al. Vcam-1 targeted nanocarriers of Shrna-Smad3 mitigate endothelial-to-mesenchymal transition triggered by high glucose concentrations and osteogenic factors in valvular endothelial cells. *Int J Biol Macromol*. 2024;281(Pt 1):136355. doi:10.1016/j.ijbiomac.2024.136355
39. Chen J, Wu W, Zhang M, Chen C. Taraxasterol suppresses inflammation in il-1beta-induced rheumatoid arthritis fibroblast-like synoviocytes and rheumatoid arthritis progression in mice. *Int Immunopharmacol*. 2019;70:274–283. doi:10.1016/j.intimp.2019.02.029
40. Mateen S, Zafar A, Moin S, Khan AQ, Zubair S. Understanding the role of cytokines in the pathogenesis of rheumatoid arthritis. *Clin Chim Acta*. 2016;455:161–171. doi:10.1016/j.cca.2016.02.010
41. Buie HR, Bosma NA, Downey CM, Jirik FR, Boyd SK. Micro-Ct evaluation of bone defects: applications to osteolytic bone metastases, bone cysts, and fracture. *Med Eng Phys*. 2013;35(11):1645–1650. doi:10.1016/j.medengphy.2013.05.016
42. Janakiraman K, Krishnaswami V, Rajendran V, Natesan S, Kandasamy R. Novel nano therapeutic materials for the effective treatment of rheumatoid arthritis-recent insights. *Mater Today Commun*. 2018;17:200–213. doi:10.1016/j.mtcomm.2018.09.011
43. Liu J, Chen X, Xu L, et al. Neutrophil membrane-coated nanoparticles exhibit increased antimicrobial activities in an anti-microbial resistant K. Pneumonia infection model. *Nanomedicine-UK*. 2023;48:102640. doi:10.1016/j.nano.2022.102640
44. Ma M, Zou F, Abudureheman B, et al. Magnetic microcarriers with accurate localization and proliferation of mesenchymal stem cell for cartilage defects repairing. *Acs Nano*. 2023;17(7):6373–6386. doi:10.1021/acsnano.2c10995

45. Sharifi S, Maleki DS, Ahmadian E, et al. A biodegradable flexible micro/nano-structured porous hemostatic dental sponge. *Nanomaterials-Basel*. 2022;12:19.
46. Sun K, Tao H, Ding T, et al. Risk factors for high-dose methotrexate associated toxicities in patients with primary central nervous system lymphoma. *J Clin Pharm Ther*. 2022;47(12):2196–2204. doi:10.1111/jcpt.13791
47. Zobeck M, Bernhardt MB, Kamdar KY, Rabin KR, Lupo PJ, Scheurer ME. Novel and replicated clinical and genetic risk factors for toxicity from high-dose methotrexate in pediatric acute lymphoblastic leukemia. *Pharmacotherapy*. 2023;43(3):205–214. doi:10.1002/phar.2779